RSC Advances

PAPER

View Article Online
View Journal | View Issue

Cite this: *RSC Adv.*, 2018, **8**, 4624

Albumin-assisted exfoliated ultrathin rhenium disulfide nanosheets as a tumor targeting and dual-stimuli-responsive drug delivery system for a combination chemo-photothermal treatment†

Qunlian Huang, Shurong Wang, Jie Zhou, Xiaoyan Zhong and Yilan Huang *

Herein, we prepared an ultrathin rhenium disulfide nanosheet ($utReS_2$) through the bovine serum albumin (BSA)-assisted ultrasonic exfoliation method, which showed great biocompatibility and high near-infrared (NIR) absorbance. The large surface specific area and the presence of BSA facilitate a high loading ratio and modification of multifunctional molecules. The low solubility anti-cancer drug resveratrol (RSV) was loaded onto the $utReS_2$ surface to form a biocompatible nanocomposite ($utReS_2$@RSV). A targeting molecule, folic acid (FA), was then conjugated to the BSA molecule of $utReS_2$@RSV, resulting in $utReS_2$@RSV–FA. The $utReS_2$@RSV–FA exhibited a photothermal effect under an 808 nm laser irradiation. At pH = 6.5, about 16.5% of the RSV molecules was released from $utReS_2$@RSV–FA over 24 h, while the value reached 55.3% after six cycles of NIR irradiation (5 min, 1 W cm^{-2}). *In vitro* experiments of $utReS_2$@RSV–FA showed that it had low cytotoxicity and an excellent HepG2 cells targeting effect. Upon pH/temperature dual-stimuli, $utReS_2$@RSV–FA showed an enhanced cytotoxic effect. *In vivo* experiments of $utReS_2$@RSV–FA intravenously injected into tumor-bearing mice showed that at 24 h post-injection, it could actively target and was largely accumulated in tumor tissue. When the injection was further accompanied by three cycles of NIR irradiation for 5 min, once a day, the tumor was efficiently suppressed, without relapse after 30 days. These findings demonstrate that $utReS_2$@RSV–FA has a remarkable targeting ability while providing a dual-stimuli-responsive drug delivery system, and could effectively be used in a combination chemo-photothermal cancer treatment.

Received 19th December 2017
Accepted 15th January 2018

DOI: 10.1039/c7ra13454a

rsc.li/rsc-advances

1. Introduction

Nowadays, cancer is undoubtedly one of the leading causes of deaths worldwide.[1] Although various cancer treatment methods are available, such as surgery, radiotherapy, and chemotherapy, their disadvantages limit their therapeutic efficacy.[2–4] For example, surgery has a potential hazard of organ malfunction and a risk of relapse when malignant cells are not completely removed;[5] radiotherapy is radiotoxic to the nearby healthy tissues;[6] and chemotherapy is toxic to nearby normal and fast dividing cells (*e.g.*, hair loss) due to its non-specificity, as well as inherent leakages of drugs to nearby healthy tissues.[7,8] In the last decades, a new and minimal invasive cancer treatment, photothermal therapy (PTT), has emerged. The therapy causes hyperthermia generated by photothermal agents (which absorb laser energy), leading to cancer cell death.[9–13] PTT has been used as a promising alternative or as a supplementary treatment to the traditional cancer therapies. However, a number of PTT research studies reported that the use of PTT on its own often has a deficiency, such as incomplete tumor suppression, which could potentially generate a tumor relapse.[14,15] Therefore, a more efficient tumor therapy strategy—simultaneous specific delivery of hyperthermia and chemotherapeutic drugs into tumor cells—has reportedly been able to overcome the shortcomings of single tumor PTT or chemotherapy. The strategy integrates multiple therapeutic abilities into a single nanoplatform.[16,17]

In addition to great biocompatibility and stability, high specific area and strong near infrared (NIR) absorbance are regarded as the most important factors for a chemo-photothermal treatment nanoplatform.[18,19] Whilst high specific area allows the nanoplatform to have a higher drug loading ratio, strong NIR absorbance facilitates the nanoplatform with increased photothermal effect.[20,21] To date, some nanomaterials, such as metal nanostructures, including noble metal-based materials (*e.g.*, Au and Pd nanomaterials) and copper-based nanoparticles, have been shown to possess strong NIR absorbance capabilities and have promising photothermal therapeutic effects demonstrated by various *in vitro* and *in vivo*

Department of Pharmacy, The Affiliated Hospital of Southwest Medical University, Luzhou, Sichuan 646000, China. E-mail: hyl_medicine@163.com; Tel: +86-18982423710

† Electronic supplementary information (ESI) available. See DOI: 10.1039/c7ra13454a

experiments.[22–24] However, further applications of these nanomaterials are limited to their low drug ratio caused by their low specific area. These issues were overcome when two-dimensional (2D) nanomaterials, including 2D carbon nanomaterials (*e.g.*, grapheme oxide and reduced grapheme oxide) and transition metal dichalcogenides (TMDCs) were developed. The materials were designed to have a large specific area and high intrinsic NIR absorbance, in addition to high drug loading, so that they can provide a more effective chemo-photothermal treatment.[25–27]

According to multiple recent research studies, a large variety of TMDCs, such as MoS_2, $MoSe_2$, WS_2, TiS_2, and Bi_2Se_3 nanosheets, have been explored and applied in biological sensing and imaging, drug delivery, and PTT.[28,29] The exfoliated TMDCs (*i.e.*, $MoSe_2$, MoS_2, WS_2, and WSe_2) have been reported to have lower cytotoxicity than the classic 2D materials (*i.e.*, graphene and its analogues).[30] A new family member to the 2D TMDCs, rhenium disulfide (ReS_2) nanosheets have been shown to have a strong NIR absorbance and are great potential NIR photothermal transducers.[31,32] Moreover, they have a large surface specific area, providing a potentially high loading ratio of the delivered drug to tumor cells.

Herein, we developed albumin-assisted exfoliated ultrathin rhenium disulfide nanosheets (utReS$_2$) with great biocompatibility, large surface specific area, and modifiable surface. Resveratrol (RSV) is a natural molecule that has been proven to have cancer preventive and therapeutic activities without any potential side effects.[33,34] In recent years, RSV has also been shown to have cytotoxic potential against liver cancer.[35] However, the disadvantages of low solubility and systemic circulation time, and non-specificity limit the practical application of RSV.[36,37] RSV was thus loaded onto the utReS$_2$ surface (utReS$_2$@RSV), which was then conjugated with a target molecule, folic acid (FA), to form a nanocomposite (utReS$_2$@RSV–FA). *In vitro* and *in vivo* experiments demonstrated that the utReS$_2$@RSV–FA had a high liver cancer targeting effect, and could be a pH/temperature dual-stimuli-responsive drug delivery system in a combination chemo-photothermal treatment (Fig. 1).

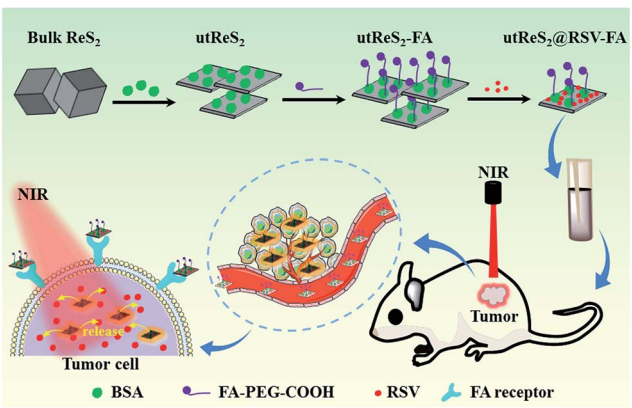

Fig. 1 A schematic illustration of the utReS$_2$@RSV–FA synthesis for tumor targeted chemo-photothermal therapy.

2. Experimental section

2.1 Materials and instruments

Rhenium disulfide (ReS_2) powder, 1-ethyl-3-(3-dimethylaminopropyl)carbodiimide (EDC) and *N*-hydroxysuccinimide (NHS), bovine serum albumin (BSA, ≥98.0%) and fluorescein isothiocyanate (FITC) were purchased from Sigma-Aldrich. Dulbecco's Modified Eagle's Medium (DMEM), fetal bovine serum (FBS) and 4′,6′-diamidino-2-phenylindole (DAPI) were obtained from Invitrogen (Carlsbad, CA, USA).

Transmission electron microscopy (TEM) images were collected on a transmission electron microscope (SU8010, Hitachi, Japan). Atomic force microscopy (AFM) images were captured by an atomic force microscope (OMCL, Olympus, Japan). The size and zeta potential of nanoparticles was detected by a nanosizer (Malvern Instruments). The UV-vis absorption spectra were detected by a UV-vis spectrophotometer (UV-2550, Shimadzu, Japan). An inductively coupled plasma optical emission spectrometer (ICP-OES, iCAP 7000 Plus, Thermo Scientific, USA) was used to measure the Re element content.

2.2 Preparation of utReS$_2$@RSV–FA

Firstly, 10 mg ReS_2 powder was mixed with 20 mL water and stirred for 20 min. Afterwards, the mixture was first ice-bath ultra-sonic dissociated using a 500 W and 20 kHz tip sonication (SONICS, VCX130, USA) for 3 h, and then was ice-bath ultrasonic dissociated (200 W, 20 kHz) in the presence of 10 mg BSA powder for 12 h. To remove large aggregates and superfluous reagents, the prepared mixture was centrifuged at 10 000 rpm for 10 min. The supernatant was collected and purified by high-speed centrifugation at 15 000 rpm for 20 min, resulting in utReS$_2$.

Secondly, 20 mg NH_2–PEG_{2000}–FA dissolved in 1 mL ethanol solution was mixed with utReS$_2$ solution and reacted for 3 h under the presence of 4 mM EDC and 10 mM NHS with stirring at room temperature and pH 6.0. To remove the unconjugated NH_2–PEG_{2000}–FA and redundant chemical reagents, the mixture was dialyzed in deionized water for 24 h, resulting in utReS$_2$–FA.

Lastly, the RSV was dissolved in DMSO, and added into 10 mL utReS$_2$–FA nanosheets water suspension with constant and slight stirring at 25 °C for 12 h. Unbound RSV was removed by dialyzing in deionized water for 24 h to give utReS$_2$@RSV–FA nanosheets, which were stored at 4 °C. The RSV loading ratio was detected *via* monitoring of the absorption peak of RSV at 306 nm and calculated according to the equation:

$$\text{RSV loading ratio } (\%) = \frac{A_a - A_b}{A_c} \times 100\%$$

where A_a (mg), A_b (mg) and A_c (mg) respectively represent the initial, unbound RSV and the ReS_2 nanosheets (mg).

2.3 Cell culture and cell uptake assay

The human hepatic HepG2 cells were obtained from the Chinese Academy of Sciences Cell Bank of Type Culture Collection (CBTCCCAS, Shanghai, China). All cells were

cultured in complete DMEM media (10% FBS + 90% DMEM) in a humidified incubator containing 5% CO_2 at 37 °C.

Firstly, $utReS_2$ nanosheets were labeled by FITC. 1 mg FITC was dissolved in 1 mL DMSO and mixed with the $utReS_2$@RSV and $utReS_2$@RSV–FA suspension with slight stirring at room temperature for 12 h. The mixture was dialyzed in deionized water for 24 h to remove the unbound FITC, resulting in purified FITC labeled $utReS_2$@RSV and $utReS_2$@RSV–FA ($utReS_2$@RSV/FITC and $utReS_2$@RSV–FA/FITC). HepG2 cells were cultured in six-well plates for 24 h and then incubated with free FITC, $utReS_2$@RSV/FITC or $utReS_2$@RSV–FA/FITC (with same FITC concentration) for 3 h. After thrice washing the cells with PBS, the cells were fixed by glutaraldehyde and stained with DAPI for 8 min. One part of the cells was used to observe the cellular fluorescence using the laser scanning microscope (LSM 510, Zeiss, Germany). The other part of the cells was collected for flow cytometry (FCM, EPICS XL, Beckman, USA) analysis to calculate the uptake ratios through counting of the cellular FITC fluorescence intensity ($E_x = 488$ nm).

2.4 *In vitro* biocompatibility

A standard CCK-8 assay (Bestbio, China) was first used to evaluate the cytotoxicity of $utReS_2$–FA. HepG2 cells (1×10^5 cells per mL) were cultured in a 96-well plate for 24 h. After removing the old media, $utReS_2$–FA (0.02, 0.05, 0.1, and 0.2 mg mL^{-1}) was incubated with HepG2 cells for 24 h. Afterwards, the cells were washed with PBS thrice mildly. According to the protocol of the CCK-8 assay, a CCK-8 working solution (100 μL) was added to each well and incubated with cells at 37 °C for 30 min. Lastly, a microplate reader (EnVision, PerkinElmer, USA) was used to detect the absorbance value at 450 nm.

In addition, mouse red blood cells (RBCs) were collected and mixed with different concentrations of $utReS_2$@RSV–FA (20, 50, 100, 200 and 400 μg mL^{-1}). After incubating at 37 °C for 1 h, the treated RBCs above were centrifuged (10 000 rpm) for 1 min. RBCs incubated with deionized water and PBS were used as the positive and negative controls, respectively. The absorbance value at 541 nm of the supernatant was measured using a UV-vis spectroscopy. The hemolytic percentage (HP) was calculated according to the equation:

$$\mathrm{HP}\ (\%) = \frac{A_t - A_{nc}}{A_{pc} - A_{nc}} \times 100\%$$

where A_t, A_{pc} and A_{nc} are the absorbance of the test samples, and positive and negative controls, respectively.

2.5 *In vitro* tumor therapy

For *in vitro* tumor therapy, HepG2 cells (5×10^4 cells per well) were cultured in 96-well plates for 24 h. Then various concentrations of $utReS_2$, RSV, and $utReS_2$@RSV–FA were added into the cell wells and incubated with the cells for an extra 24 h. The cell viability was detected by CCK-8 assay as mentioned above. For *in vitro* PTT, various concentrations of $utReS_2$, RSV, and $utReS_2$@RSV–FA treated cells were irradiated using the 808 nm laser (1 W cm^{-2}) for 5 min. The real-time temperature and thermal images (once every 30 seconds) of the cells were first recorded by the thermocouple thermometer (BAT-7001H, Physitemp, USA) and infrared thermal camera (TI25, FLUKE, USA), respectively. These cells were the continuously cultured for 24 h. The cell viabilities were also evaluated by the CCK-8 assay. Simultaneously, these cells were co-stained by calcein-AM/PI (Aladdin, Shanghai, China) for 30 min and then imaged using a confocal laser scanning microscope (calcein-AM $E_x = 488$ nm, PI $E_x = 535$ nm).

2.6 Animal model and *in vivo* biodistribution

To establish the HepG2 subcutaneous tumor model, 1×10^7 HepG2 cells (100 μL, in PBS) were subcutaneously injected into the back of Balb/c nude mice. The tumor volume was established by: tumor volume = length × $width^2/2$. All animal procedures were performed in accordance with the Guidelines for Care and Use of Laboratory Animals of the National Institutes of Health (NIH publication no. 85-23, revised 1996) and approved by the Animal Ethics Committee of Southwest Medical University (Luzhou, China).

Biodistribution of $utReS_2$@RSV and $utReS_2$@RSV–FA in the tumor-bearing nude mice was detected at 1 h, 1 day, 2 days, 5 days and 7 days post tail intravenous injection with these samples (100 μL). The major organs, including the heart, liver, spleen, lung, kidney, and tumor, were weighed and digested by aqua regia solution. The Re element content in these tissues was quantified by ICP-OES.

2.7 *In vivo* anticancer efficacy and toxicity study

In the *in vivo* anticancer experiments, the tumor-bearing nude mice were randomly divided into six groups ($n = 7$): (1) PBS (100 μL); (2) PBS (100 μL) + NIR laser; (3) RSV (100 μL, 4 mg kg^{-1}); (4) $utReS_2$@RSV (100 μL, 2 mg kg^{-1}) + NIR laser; (5) $utReS_2$@RSV–FA and $utReS_2$@RSV–FA (100 μL, 4 mg kg^{-1} RSV and 2 mg kg^{-1} ReS_2) + NIR laser. After 24 h intravenous injection, the tumor region of the tumor bearing mice in these groups was irradiated by NIR laser (1 W cm^{-2}, 5 min) once a day for three days. The temperature of the tumor region in the NIR irradiated groups was recorded. During the treatment, the tumor volume and body weight were recorded every three days. The relative tumor volume was calculated by: relative tumor volume = V/V_0, in which V_0 was the tumor volume when the tumor treatment was initiated.

For the *in vivo* toxicity study, healthy Balb/c mice were intravenously injected with $utReS_2$@RSV–FA (10 mg kg^{-1}) or an equal volume of saline. The major organs, including the lung, heart, liver, spleen, and kidney were harvested for histological analysis after 15 days. The H&E images were obtained using a digital camera. In addition, whole blood samples of these mice were collected at 1, 7 and 30 days after injection for blood analysis. The complete blood counts, including white blood cell count (WBC), red blood cell count (RBC), hemoglobin concentration (HGB), mean platelet volume (MPV), hematocrit (HCT), mean corpuscular volume (MCV), and mean corpuscular hemoglobin concentration (MCHC) were detected using a hemocytometer (Countess C10227, Invitrogen, USA).

3. Results and discussion

3.1 Synthesis and characterization of utReS$_2$@RSV–FA

An observation by TEM showed that the utReS$_2$@RSV–FA had a flake-like morphology with a lattice spacing of 0.23 nm (Fig. 2a and b), similar to the morphology of the utReS$_2$ nanosheets (Fig. S1†), this indicates that it has an ultrathin structure. According to AFM analysis (Fig. 2c and d), the center thickness (~7.6 nm) of utReS$_2$@RSV–FA increased compared to the edge thickness (~2 nm), which is likely due to BSA adhesion, RSV loading, and FA conjugation. The utReS$_2$@RSV–FA had an average diameter of about 150 nm and an average zeta potential of −32 mV, as evaluated by a nanosizer (Fig. 2e and f).

As shown in Fig. 3a, compared with that of the bulk ReS$_2$, the absorption spectrum of the BSA-assisted exfoliated utReS$_2$ exhibited a new peak at 275 nm (originating from the BSA) (Fig. S2†), indicating the presence of BSA in utReS$_2$. The absorption spectrum of the utReS$_2$@RSV–FA (displayed in Fig. 3b) showed a peak associated with RSV at 306 nm and a high NIR absorbance, demonstrating that RSV was successfully loaded onto the utReS$_2$ nanosheets. In addition, a significant fluorescence quenching was observed after RSV was loaded onto the utReS$_2$ surface (Fig. 3c), indicating further interactions between utReS$_2$ and RSV. As a 2D material that is similar to graphene,[2] utReS$_2$ nanosheets have large surface areas; they can therefore load and bind functional molecules through non-covalent interactions (*e.g.*, π–π stacking and hydrophobic interactions). The loading capacities of utReS$_2$ nanosheets increased with the increase of RSV concentrations (Fig. 3d), and reached the highest RSV loading ratio of ~200% (w/w). Moreover, compared to utReS$_2$, bulk ReS$_2$ showed a lower drug loading ratio (~45.6%) (Fig. 3d). The high drug loading ratio may be due to the large surface specific area and BSA adhesion of utReS$_2$. Fig. 3e shows that the average sizes of utReS$_2$@RSV–FA in water, FBS, cell media, PBS, and saline were almost unchanged over 7 days, suggesting that utReS$_2$@RSV–FA has a high stability, possibly due to BSA adhesion and PEG conjugation on the utReS$_2$ surface. According to the literature, RSV has two natural isomers, *cis* and *trans* (*trans* has a higher bioactivity and stability than the *cis* configurations), which exhibit featured absorbance peaks at 280 and 304 nm, respectively.[38] In this regard, the change of ratio of $A_{304\ nm}$ to $A_{280\ nm}$ ($A_{304\ nm}/A_{280\ nm}$) represents the interconversion between the two isomers. As illustrated in Fig. 3f, the $A_{304\ nm}/A_{280\ nm}$ ratio was nearly unchanged for 7 days, demonstrating that RSV has a *trans*-configuration and remains stable in utReS$_2$@RSV–FA.

Fig. 4a shows the schematic illustration of the pH/temperature stimuli-responsive RSV release. As shown in Fig. 4b, the temperature of the utReS$_2$@RSV–FA solution was concentration-dependent, varying with different concentrations (0–200 ppm) upon an 808 nm irradiation (1 W cm^{-2}, 5 min). The utReS$_2$@RSV–FA of 200 ppm irradiated with NIR reached a maximum temperature of ~60 °C. After five cycles of NIR irradiation, the initial photothermal effects of utReS$_2$@RSV–FA remained (Fig. 4c). Moreover, its absorbance spectra before and after five cycles of NIR irradiation were similar (Fig. S3†). According to the literature method,[9] the photothermal conversion efficiency of utReS$_2$@RSV–FA was calculated to be 45.1%. These results indicate the utReS$_2$@RSV–FA has great photostability and an excellent photothermal effect. Fig. S4† shows that normal and inner tumor tissues have a pH of about 7.4 and 6.5, respectively. The pH in cellular lysosome is also acidic. Fig. 4d shows the RSV release ratio in response to various pH and irradiation conditions. The 24 h release of RSV from utReS$_2$@RSV–FA was 7.6% at a physiological pH of 7.4, while that was significantly increased to 16.5% at pH 6.5. With the

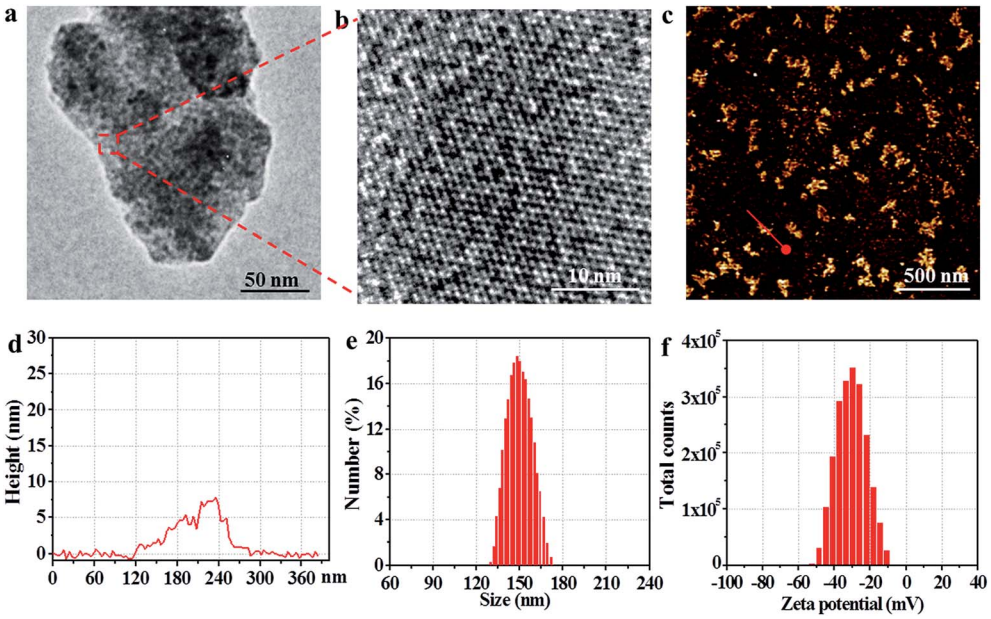

Fig. 2 (a) The TEM image of utReS$_2$@RSV–FA. (b) The high-resolution TEM image of the red dashed frame region in (a). (c) The typical AFM image of utReS$_2$@RSV–FA. (d) The height profile of the red line region in (c). The (e) size and (f) zeta potential distribution of utReS$_2$@RSV–FA.

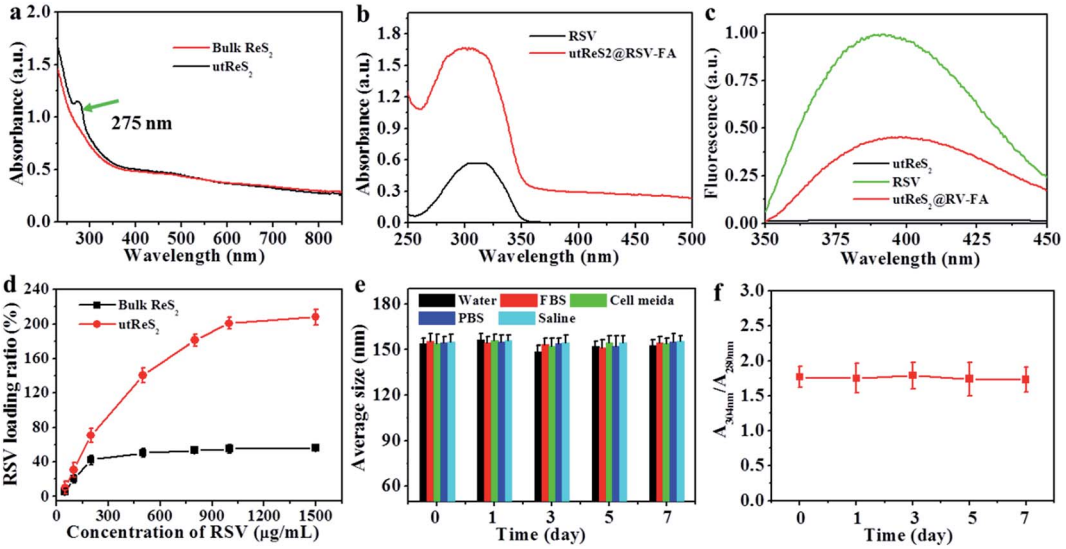

Fig. 3 (a) The absorption spectra of the bulk ReS_2 and $utReS_2$ nanosheets. (b) The absorption spectra of RSV and $utReS_2$@RSV–FA. (c) The fluorescence spectra of $utReS_2$, RSV and $utReS_2$@RSV–FA. (d) RSV loading ratio onto bulk ReS_2 and $utReS_2$ as the function of added RSV concentrations. (e) The average size change of $utReS_2$@RSV–FA in water, FBS, cell media, PBS and saline over 7 days. (f) The absorbance ratio change of $utReS_2$@RSV–FA between 304 nm and 280 nm ($A_{304\ nm}/A_{280\ nm}$) over 7 days.

decrease of the pH value (pH = 7.4–3.0), the cumulative released RSV increased obviously (Fig. S5†). In addition, with irradiation for 5 min (808 nm, 1 W cm^{-2}), the RSV release was about 25.1% at pH 7.4 (Fig. S6†), indicating that weak acid conditions and photothermal effects could promote the RSV release. At pH 6.5, and irradiation (808 nm, 1 W cm^{-2}) for 5 min, the RSV release was significantly increased to 55.3%, which was much higher than that without irradiation. These results indicate that the weak acidic environment in tumors and the controllable external photothermal effect could be used as a dual-stimuli controlling an on/off release of RSV from $utReS_2$@RSV–FA. RSV was released from the $utReS_2$ surface due to heat generated by $utReS_2$ upon absorption of NIR light, and such heat could weaken the non-covalent

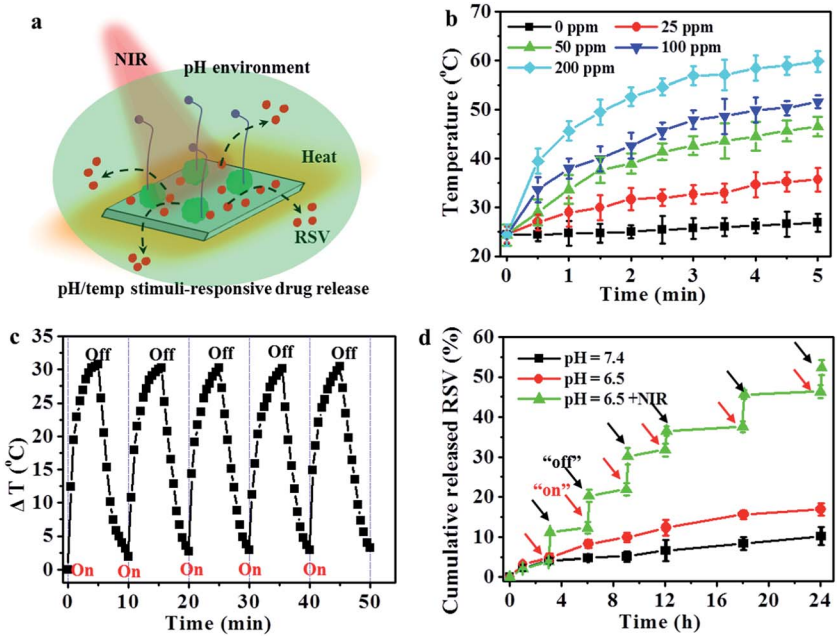

Fig. 4 (a) The schematic illustration of pH/temperature (pH/temp) stimuli-responsive drug release. (b) Temperature curves of the $utReS_2$@RSV–FA solution (0, 25, 50, 100 and 200 ppm) under laser irradiation (5 min, 808 nm, 1 W cm^{-2}). (c) Temperature changes of $utReS_2$@RSV–FA after 5 cycles of irradiations (5 min, 808 nm, 1 W cm^{-2}). (d) Release kinetics of RSV from $utReS_2$@RSV–FA in pH = 7.4 and 6.5 with or without NIR laser irradiation, respectively.

adsorption interactions between RSV and $utReS_2$ surface.[3] In addition, in an acidic environment, the H^+ could change the surface charge of $utReS_2$, altering the hydrophilic/hydrophobic balance of the nanoparticles.[39–41]

3.2 *In vitro* cell uptake and biocompatibility

The $utReS_2$@RSV–FA could target HepG2 cells through the FA receptor (Fig. 5a). Fluorescein isothiocyanate was used to label the $utReS_2$@RSV–FA, and its fluorescence signal was observed through a fluorescence microscope. As shown in Fig. 5b, $utReS_2$@RSV–FA-treated cells had a stronger green FITC fluorescence in the cytoplasm than the $utReS_2$@RSV- and free-FITC-treated cells. After FA blocking, the $utReS_2$@-RSV–FA-treated cells showed weaker green FITC fluorescence inside the cytoplasm, indicating that the FA receptor on the cell membrane is hindered (by free FA), in turn, this reduces the targeting ability and accessibility of $utReS_2$@RSV–FA. The quantitative cellular uptake ratio of $utReS_2$@RSV–FA according to FCM was about 61.1%, which was higher than that of free FITC (2.1%), $utReS_2$@RSV (23.5%), and $utReS_2$@RSV–FA + FA (19.7%) (Fig. 5c). The results demonstrated that the FA conjugation could promote the cell internalization of $utReS_2$@RSV–FA through the receptor-mediated endocytosis.[42]

In vitro biocompatibility of $utReS_2$–FA, as a drug carrier, was evaluated by cell viability and hemolysis of red blood cells (RBCs). As shown in Fig. 5d, the viabilities of the HepG2 cells treated with 0–200 μg mL^{-1} were more than 95%, indicating that $utReS_2$–FA has a very low cytotoxicity. Fig. 5e illustrates that the hemolysis ratio of $utReS_2$–FA at a concentration range of 20 to 400 μg mL^{-1} was similar to that of the negative control, suggesting that the $utReS_2$–FA has good hemocompatibility, which could be ascribed to the conjugated BSA and PEG in $utReS_2$.

3.3 *In vitro* tumor therapy

Fig. 6a shows the temperature of adherent HepG2 cells incubated with PBS, $utReS_2$, $utReS_2$@RSV, and $utReS_2$@RSV–FA solutions (50 μg mL^{-1} with respect to $utReS_2$) under an 808 nm irradiation (1.0 W cm^{-2}) for 5 min. The results showed that cells treated with $utReS_2$@RSV–FA had the highest temperature increase (ΔT = 25 °C) compared to $utReS_2$, $utReS_2$@RSV, and

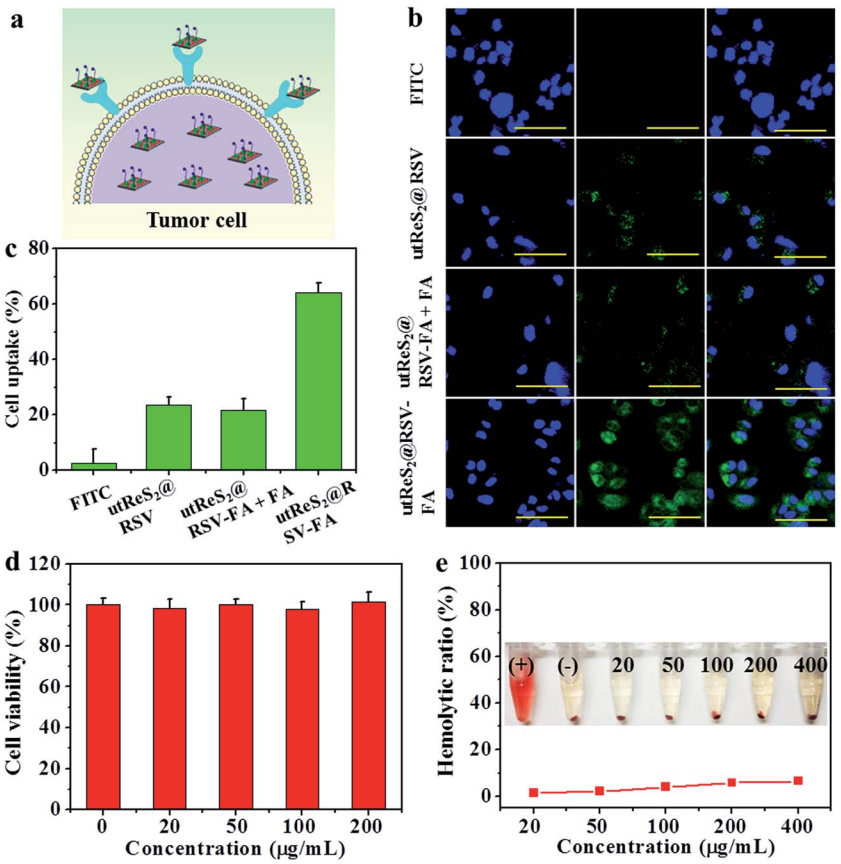

Fig. 5 (a) The schematic illustration of $utReS_2$@RSV–FA target to tumor cell mediated by the FA receptor. (b) Fluorescence images of HepG2 cells after incubation with free FITC and $utReS_2$@RSV, $utReS_2$@RSV–FA + FA and $utReS_2$@RSV–FA (labeled with FITC). Green and blue colors are FITC and DAPI fluorescence, respectively. Scale bar = 20 μm. (c) Flow cytometry quantitative results of cellular FITC fluorescence in HepG2 cells. (d) *In vitro* cytotoxicity against HepG2 cells treated with different concentrations of ReS_2–FA. (e) Hemolytic ratio of RBCs after 1 hour incubation with $utReS_2$@RSV–FA at different concentrations. The inset shows the photograph of water (+), PBS (–), and different concentrations of $utReS_2$@RSV–FA treated RBCs.

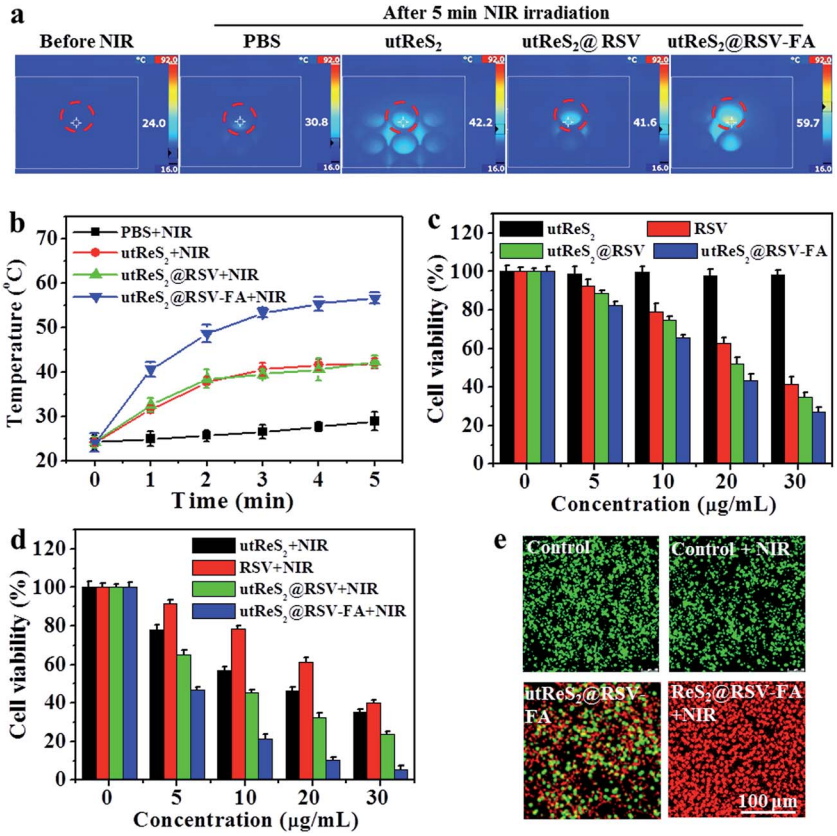

Fig. 6 (a) Thermal images of PBS, $utReS_2$, $utReS_2$@RSV and $utReS_2$@RSV–FA treated cells in 96-well plates after 5 min NIR irradiation, and (b) the corresponding temperature change curves. (c and d) Viability of the cells treated with RSV, $utReS_2$, $utReS_2$@RSV and $utReS_2$@RSV–FA with or without 808 nm laser irradiation (5 min, 1 W cm^{-2}). (e) The calcium AM/PI dual-staining images of cells after treatment by control (PBS), control + NIR, $utReS_2$@RSV–FA and $utReS_2$@RSV–FA + NIR, respectively.

PBS-treated cells (Fig. 6b). The viabilities of cells treated with various concentrations of $utReS_2$, RSV, $utReS_2$@RSV, and $utReS_2$@RSV–FA for 24 h without NIR irradiation were concentration-dependent, the viability decreased with increasing concentration (except for $utReS_2$). The highest cell viability of 32.1 ± 1.2% was observed in $utReS_2$@RSV–FA-treated cells (Fig. 6c). In contrast, significant concentration-dependent cell deaths were observed in cells treated with $utReS_2$, $utReS_2$@RSV, and $utReS_2$@RSV–FA under a NIR irradiation (1.0 W cm^{-2}, 5 min) (Fig. 6d). The effect was particularly significant in $utReS_2$@RSV–FA-treated cells. It is possible that such *in vitro* PTT effect is due to FA targeting, which promotes the internalization of $utReS_2$@RSV–FA, thus generating more heat upon NIR irradiation, releasing more drugs, and enhancing the cytotoxicity effects.

Furthermore, calcein-AM/PI dual staining was further used to investigate the cytotoxic effect of $utReS_2$@RSV–FA with or without NIR irradiation. Both the control and the control + NIR cells exhibited green fluorescence, indicating that the laser irradiation has no effects on the cells (Fig. 6e). Cells treated with $utReS_2$@RSV–FA without irradiation were partially dead, exhibiting red fluorescence, whereas those with irradiation were almost completely dead (Fig. 6e). The results corresponded with those from the CCK-8 assay (Fig. 6d).

3.4 *In vivo* biodistribution and chemo-photothermal combination treatment

Understanding the biodistribution of nanoparticles in major organs (*i.e.*, heart, liver, spleen, lung, and kidney) as well as tumors can guide *in vivo* combination chemo-photothermal cancer treatments. At 24 h post-injection, tumor-bearing mice intravenously injected with $utReS_2$@RSV–FA exhibited higher accumulation (of the corresponding injected nanoparticles in tumor cells) than those injected with $utReS_2$@RSV (Fig. 7a). The nanoparticles were accumulated in liver and spleen, in addition to tumor (Fig. 7b), suggesting that the nanoparticles may be metabolized in the liver and kidney. These observations suggest that the FA targeting enhances the accumulation of nanoparticles in the tumor.

In addition, Fig. 7c shows the tumor temperature of tumor-bearing mice intravenously injected with PBS, $utReS_2$, $utReS_2$@RSV, and $utReS_2$@RSV–FA at 24 h post-injection under an 808 nm laser irradiation (1 W cm^{-2}) for 5 min. The highest temperature increase (by about 21 °C) was observed in $utReS_2$@RSV–FA-treated tumor regions. After three cycles of NIR irradiation (once a day) and subsequent treatment for about one month, the groups treated with PBS, PBS + NIR, RSV, $utReS_2$@RSV + NIR, and $utReS_2$@RSV–FA exhibited no clear indication of tumor suppression. As expected, the

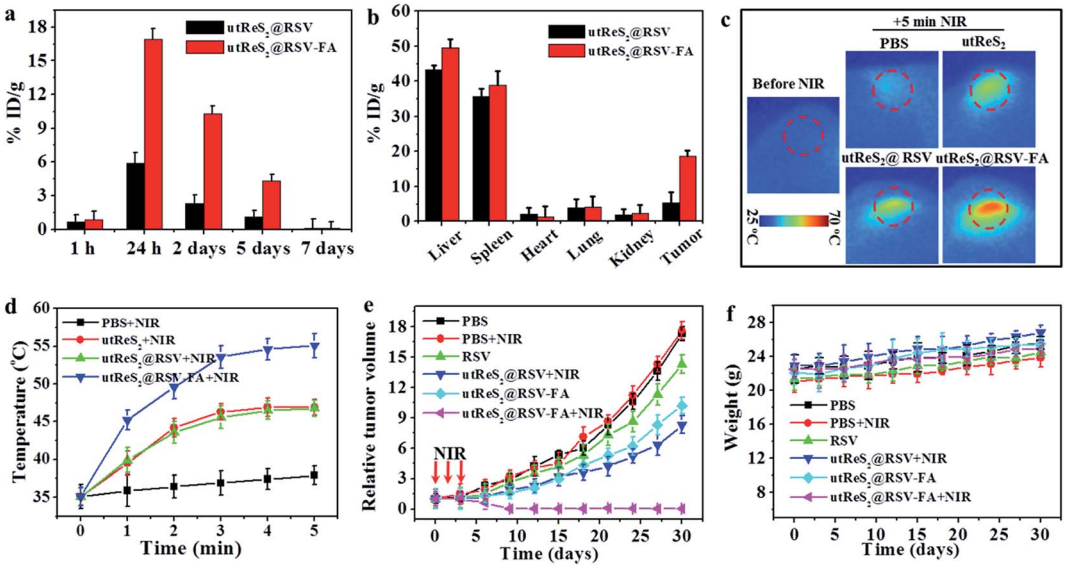

Fig. 7 (a) Biodistribution of the nanoparticles in the tumor tissue post-injection with utReS$_2$@RSV and utReS$_2$@RSV–FA. (b) Biodistribution of the nanoparticles in the major organs (*i.e.*, heart, liver, spleen, lung, kidney) as well as tumors at 24 h post-injection with utReS$_2$@RSV and utReS$_2$@RSV–FA. (c) The thermal images of tumor-bearing mice at 24 h post-injection of PBS, utReS$_2$, utReS$_2$@RSV and utReS$_2$@RSV–FA under 5 min NIR irradiation (808 nm, 1 W cm^{-2}), respectively. (d) The temperature statistical results of tumor regions of tumor-bearing mice post tail vein injection of PBS, utReS$_2$, utReS$_2$@RSV and utReS$_2$@RSV–FA at 24 h under 5 min NIR irradiation (808 nm, 1 W cm^{-2}), respectively. (e) The growth profile of HepG2 tumors after intravenous injection of PBS, RSV, utReS$_2$@RSV and utReS$_2$@RSV–FA with or without three cycles of NIR irradiation (5 min, 808 nm, 1 W cm^{-2}) once a day. (f) Body weight of tumor-bearing mice during 30 days of treatment.

utReS$_2$@RSV–FA + NIR laser group exhibited significant tumor growth suppression without a relapse (Fig. 7e). During the treatment, the decrease of mice's body weight was not significant, indicating that the injection dose was within a biosafe range. These observations illustrate that the utReS$_2$@RSV–FA with FA targeting and pH/temperature dual-stimuli RSV release possessed a high anticancer effect in the combination chemo-photothermal treatment.

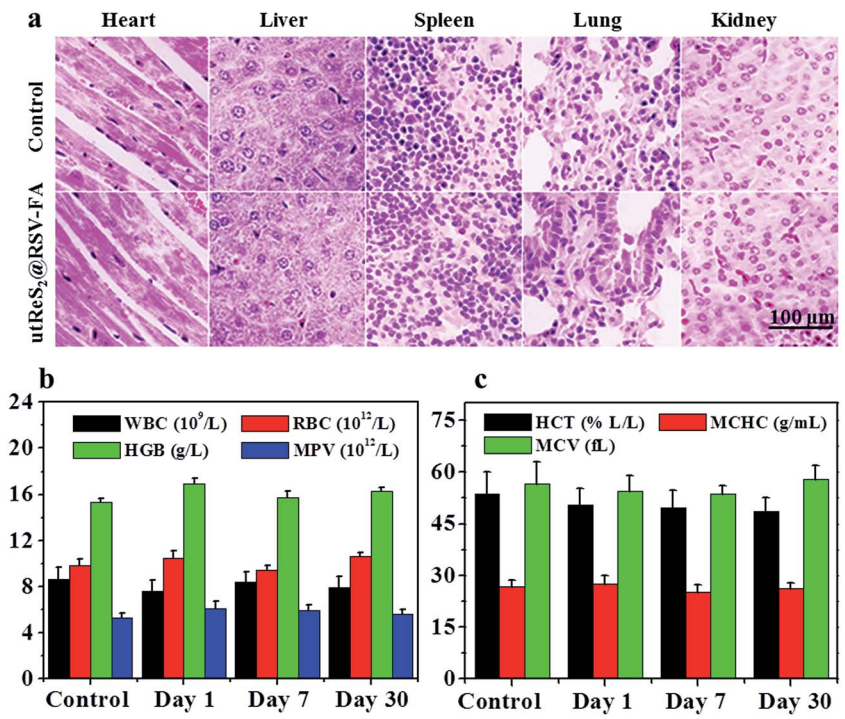

Fig. 8 (a) H&E-stained images of heart, liver, spleen, lung, and kidney from mice treated with saline (control) or utReS$_2$@RSV–FA at days 30. (b and c) Blood cells count of mice at days 1, 7 and 30 post-injection of saline (control) and utReS$_2$@RSV–FA.

3.5 *In vivo* toxicity study

In vivo toxicity of utReS$_2$@RSV–FA was further evaluated. Healthy Balb/c mice were intravenously injected with utReS$_2$@RSV–FA (10 mg kg^{-1}) or an equal volume of saline (control). Major organs, including the lung, heart, liver, spleen, and kidney, were harvested for histological analysis after 15 days. As shown in Fig. 8a, the H&E stained sections of all mice (both utReS$_2$@RSV–FA-injected and control) showed that there was no noticeable organ damage. Moreover, whole blood samples of these mice were collected at 1, 7, and 30 days post-injection for blood analysis. As illustrated in Fig. 8b and c, the complete blood counts (WBC, RBC, HGB, MPV, HCT, MCV, and MCHC) of the utReS$_2$@RSV–FA-injected mice were within the normal ranges, and were not significantly different from the control. The results demonstrate that the utReS$_2$@RSV–FA has no significant cytotoxicity *in vivo*, which indicates its excellent biocompatibility.

4. Conclusions

In summary, we prepared utReS$_2$, a new family member of TMDCs, as a tumor targeting and dual-stimuli-responsive drug delivery system in a combination chemo-photothermal treatment. The utReS$_2$, prepared by a facile albumin-assisted exfoliation method, exhibited high stability in aqueous media and great biocompatibility, in addition to excellent NIR absorbance and large surface area. It could thus induce a high photothermal effect and increase the drug-loading ratio *via* a non-covalent interaction. The utReS$_2$@RSV–FA possessed a controllable drug release in response to heat induced by a NIR laser irradiation and the endogenous weak acidic conditions of tumor tissue. FA targeting promoted the accumulation of utReS$_2$@RSV–FA in tumor cells both *in vitro* and *in vivo*. The tumor-targeted utReS$_2$@RSV–FA accompanied with NIR-mediated hyperthermia and pH/temperature-triggered RSV release showed a remarkable synergistic inhibition of tumor growth without a relapse both *in vitro* and *in vivo*. The results also confirmed that utReS$_2$@RSV–FA was not toxic to healthy tissues within the experimental dosage. These findings demonstrate that the utReS$_2$@RSV–FA prepared in this study could be a potential and high-efficiency nanoplatform for cancer therapy.

Conflicts of interest

The authors report no conflicts of interest in this work.

Acknowledgements

This work was supported by the fund of the Sichuan Provincial Science and Technology Department – Luzhou People's Government – Luzhou Medical College Joint Research Project [2014] No. 10.

References

1 Y. Liu, K. Ai, J. Liu, M. Deng, Y. He and L. Lu, *Adv. Mater.*, 2013, **25**, 1353–1359.
2 J. Chen, H. Liu, C. Zhao, G. Qin, G. Xi, T. Li, X. Wang and T. Chen, *Biomaterials*, 2014, **35**, 4986–4995.
3 R. Deng, H. Yi, F. Fan, L. Fu, Y. Zeng, Y. Wang, Y. Li, S. Ji and Y. Su, *RSC Adv.*, 2016, **6**, 77083–77092.
4 F. M. Kievit and M. Zhang, *Acc. Chem. Res.*, 2011, **44**, 853–862.
5 D. S. Chauhan, S. Indulekha, R. Gottipalli, B. P. K. Reddy, T. R. Chikate, R. Gupta, D. N. Jahagirdar, R. Prasad, A. De and R. Srivastava, *RSC Adv.*, 2017, **7**, 44026–44034.
6 H. Yue, J. Qian, V. M. Elner, J. Guo, Y. F. Yuan, R. Zhang and Q. Ge, *Br. J. Ophthalmol.*, 2013, **97**, 739–745.
7 M. L. Mancini and S. T. Sonis, *Front. Pharmacol.*, 2014, **5**, 51.
8 A. Maji and D. Sen, *Curr. Cancer Ther. Rev.*, 2017, **13**, 43–62.
9 J. Chen, X. Wang and T. Chen, *Nanoscale Res. Lett.*, 2014, **9**, 86.
10 X. Song, H. Gong, S. Yin, L. Cheng, C. Wang, Z. Li, Y. Li, X. Wang, G. Liu and Z. Liu, *Adv. Funct. Mater.*, 2014, **24**, 1194–1201.
11 P. Huang, J. Lin, W. Li, P. Rong, Z. Wang, S. Wang, X. Wang, X. Sun, M. Aronova, G. Niu, R. D. Leapman, Z. Nie and X. Chen, *Angew. Chem., Int. Ed.*, 2013, **125**, 14208–14214.
12 Q. Chen, C. Wang, L. Cheng, W. He, Z. Cheng and Z. Liu, *Biomaterials*, 2014, **35**, 2915–2923.
13 M. A. Mackey, M. R. K. Ali, L. A. Austin, R. D. Near and M. A. El-Sayed, *J. Phys. Chem. B*, 2014, **118**, 1319–1326.
14 N. Kuthala, R. Vankayala, Y. N. Li, C. S. Chiang and K. C. Hwang, *Adv. Mater.*, 2017, **29**, 1700850.
15 C. Ayala-Orozco, C. Urban, S. Bishnoi, A. Urban, H. Charron, T. Mitchell, M. Shea, S. Nanda, R. Schiff, N. Halas and A. Joshi, *J. Controlled Release*, 2014, **191**, 90–97.
16 S. Shen, H. Tang, X. Zhang, J. Ren, Z. Pang, D. Wang, H. Gao, Y. Qian, X. Jiang and W. Yang, *Biomaterials*, 2013, **34**, 3150–3158.
17 X. Wang, Q. Zhang, L. Zou, H. Hu, M. Zhang and J. Dai, *RSC Adv.*, 2016, **6**, 20949–20960.
18 J. T. Robinson, S. M. Tabakman, Y. Liang, H. Wang, H. S. Casalongue, D. Vinh and H. Dai, *J. Am. Chem. Soc.*, 2011, **133**, 6825–6831.
19 W. Yin, L. Yan, J. Yu, G. Tian, L. Zhou, X. Zheng, X. Zhang, Y. Yong, J. Li, Z. Gu and Y. Zhao, *ACS Nano*, 2014, **8**, 6922–6933.
20 X. Sun, Z. Liu, K. Welsher, J. T. Robinson, A. Goodwin, S. Zaric and H. Dai, *Nano Res.*, 2008, **1**, 203–212.
21 D. P. O'Neal, L. R. Hirsch, N. J. Halas, J. D. Payne and J. L. West, *Cancer Lett.*, 2004, **209**, 171–176.
22 W. Fang, S. Tang, P. Liu, X. Fang, J. Gong and N. Zheng, *Small*, 2012, **8**, 3816–3822.
23 M. Chen, S. Tang, Z. Guo, X. Wang, S. Mo, X. Huang, G. Liu and N. Zheng, *Adv. Mater.*, 2014, **26**, 8210–8216.
24 M. Everts, V. Saini, J. L. Leddon, R. J. Kok, M. Stoff-Khalili, M. A. Preuss, C. L. Millican, G. Perkins, J. M. Brown, H. Bagaria, D. E. Nikles, D. T. Johnson, V. P. Zharov and D. T. Curiel, *Nano Lett.*, 2006, **6**, 587–591.

25 T. Liu, C. Wang, X. Gu, H. Gong, L. Cheng, X. Shi, L. Feng, B. Sun and Z. Liu, *Adv. Mater.*, 2014, **26**, 3433–3440.
26 C. Tan and H. Zhang, *Chem. Soc. Rev.*, 2015, **44**, 2713–2731.
27 Z. Liu, J. T. Robinson, S. M. Tabakman, K. Yang and H. Dai, *Mater. Today*, 2011, **14**, 316–323.
28 J. Chen, C. Liu, D. Hu, F. Wang, H. Wu, X. Gong, X. Liu, L. Song, Z. Sheng and H. Zheng, *Adv. Funct. Mater.*, 2016, **26**, 8715–8725.
29 G. Song, C. Liang, H. Gong, M. Li, X. Zheng, L. Cheng, K. Yang, X. Jiang and Z. Liu, *Adv. Mater.*, 2015, **27**, 6110–6117.
30 W. Z. Teo, E. L. K. Chng, Z. Sofer and M. Pumera, *Chemistry*, 2014, **20**, 9627–9632.
31 K. Keyshar, Y. Gong, G. Ye, G. Brunetto, W. Zhou, D. P. Cole, K. Hackenberg, Y. He, L. Machado, M. Kabbani, A. H. C. Hart, B. Li, D. S. Galvao, A. George, R. Vajtai, C. S. Tiwary and P. M. Ajayan, *Adv. Mater.*, 2015, **27**, 4640–4648.
32 S. Shen, Y. Chao, Z. Dong, G. Wang, X. Yi, G. Song, K. Yang, Z. Liu and L. Cheng, *Adv. Funct. Mater.*, 2017, **27**, 1700250.
33 M. R. Vijayakumar, R. Kosuru, S. K. Singh, C. B. Prasad, G. Narayan, M. S. Muthu and S. Singh, *RSC Adv.*, 2016, **6**, 74254–74268.
34 H. R. Gwak, S. Kim, D. N. Dhanasekaran and Y. S. Song, *Cancer Lett.*, 2016, **371**, 347–353.
35 Q. Jiang, M. Yang, Z. Qu, J. Zhou and Q. Zhang, *BMC Complementary Altern. Med.*, 2017, **17**, 477.
36 S. Tortorella and T. C. Karagiannis, *Curr. Drug Delivery*, 2014, **11**, 427–443.
37 S. Das, H. S. Lin, P. C. Ho and K. Y. Ng, *Pharm. Res.*, 2008, **25**, 2593–2600.
38 Y. Xin, T. Liu and C. Yang, *Int. J. Nanomed.*, 2016, **11**, 5807–5821.
39 Y. Chen, C. Tan, H. Zhang and L. Wang, *Chem. Soc. Rev.*, 2015, **44**, 2681–2701.
40 Y. Zhu, J. Shi, W. Shen, X. Dong, J. Feng, M. Ruan and Y. Li, *Angew. Chem., Int. Ed.*, 2005, **117**, 5213–5217.
41 D. Schmaljohann, *Adv. Drug Delivery Rev.*, 2006, **58**, 1655–1670.
42 S. K. Jones, A. Sarkar, D. P. Feldmann, P. Hoffmann and O. M. Merkel, *Biomaterials*, 2017, **138**, 35–45.